Journal of Quantitative Spectroscopy & Radiative Transfer 322 (2024) 109018

Contents lists available at ScienceDirect

Journal of Quantitative Spectroscopy and Radiative Transfer

journal homepage: www.elsevier.com/locate/jqsrt

A light scattering analysis of the cryovolcano plumes on enceladus

Claudia Morello *, Matthew J. Berg

Kansas State University, Department of Physics, 1228N Martin Luther King Dr, Manhattan, KS, 66506-2601, USA

ARTICLE INFO

Keywords:
Enceladus
Light scattering
Cryovolcano
Mean anomaly
Q-space

ABSTRACT

Observations by NASA's Cassini spacecraft show that Enceladus, the sixth largest moon of Saturn, has cryovolcanoes on its south pole as well as a global subsurface ocean beneath Enceladus's icy crust. Photographs from the Imaging Science Subsystem (ISS) cameras aboard Cassini during flybys of Enceladus show cryovolcano plumes. The images are taken in several filters and with linear polarizers at various angles and orbital positions. Light scattered by the plume particles and observed by Cassini may provide information about the plume composition and potentially the dynamics of the ocean below. Here, we remove the coupling between orbital position and scattered plume intensity as well as analyze ISS data using light scattering models and the Q-space method. We suggest that the plume particles are generally larger than two microns in radius and nonspherical in shape.

1. Introduction

Enceladus is the sixth largest of Saturn's many moons and is situated in Saturn's E-ring. The E-ring is the most diffuse of the rings as it is comparatively dim yet covers a large volume [1–3]. Saturn has over one hundred confirmed moons, and these all apply forces to Enceladus at varying amounts along its orbit [4]. Enceladus is thus geologically active, caused by a surplus of internal energy due to tidal friction [5]. Like Earth, this internal energy is released via volcanism, though unlike Earth, the cryovolcanoes on Enceladus are congregated near the moon's south pole [6].

Moreover, Cassini found evidence that Enceladus has a subsurface ocean [7,8]. As Enceladus is situated past the solar system's ice line, which lies between Mars and Jupiter, its surface is entirely frozen. This means that Enceladus is a rocky body with a global ocean, all enveloped by an icy crust. Given that the origin of life on Earth is thought have occurred at the hydrothermal vents, Enceladus is thus of interest as a possible host for life due to the similar geology [9,10].

In 2004, the Cassini spacecraft first observed these cryovolcanoes, or geysers, whereafter, further flybys were conducted. In the literature, the words geysers and cryovolcanoes are used interchangeably, as there is no conclusive evidence thus far on the nature of the eruption mechanism, which is what differentiates the terms. It is known, however, that they are not like terrestrial volcanoes, emitting a mixture of ice, dust, and gas as opposed to lava and ash [11]. Studies have attempted to estimate the size and shape of the plume particles, using methods like mass spectroscopy and plume particle trajectory calculations [6,12-14]. Most studies that involve light scattering analysis model the plume particles as spheres, or sphere-like shapes such as ellipsoids or aggregated spheres [10,15-17]. Yet, the frozen character of the particles suggests more complex particle morphology which is supported by our study below.

Whereas most light scattering analysis plots scattered intensity I vs scattering angle Θ, see Fig. 1, Q-space analysis plots intensity against the scattering wave vector, defined as:

$$q = 2k\sin\left(\frac{\Theta}{2}\right), \tag{1}$$

where $k = \frac{2\pi}{\lambda}$ is the wavenumber and λ is the wavelength.

Plotting the scattered intensity versus q on a log-log plot reveals power-law descriptions of the scattering with length scale dependent crossovers between power-law regimes. It also systematically describes the magnitude of the scattered intensity and the interference ripple structure that often forms the foundation of those power laws [18]. The analysis can apply to many particle shapes, from spheres, cylinders, and fractal aggregates to more complex geometries. Q-space analysis uncovers hidden information and can be used to estimate particle size and sometimes shape as well.

Q-space analysis can be helpful in remote sensing problems because Q-space analysis focuses mainly on data behavior and is not as affected by high error in the measurements. This work applies Q-space analysis to the cryovolcano observations of Enceladus. It is known that smaller

* Corresponding author.
E-mail address: morelloc@phys.ksu.edu (C. Morello).

https://doi.org/10.1016/j.jqsrt.2024.109018
Received 21 August 2023; Received in revised form 10 April 2024; Accepted 22 April 2024
Available online 23 April 2024

plume-particles escape to Saturn's E-ring and larger particles fall back to Enceladus' surface [11,19]. Water ice [20,21], nitrogen and oxygen-bearing compounds [22], sodium salts [23], silica [24], ammonia hydrate [13,14], and more recently, phosphates [25] and HCN [26], have all been detected, but many unanswered questions about the particles remain. The size distributions and possible particle geometries found by different studies vary, and no clear consensus exists. An improved understanding of the cryovolcano plumes may provide further insight for the subsurface dynamics.

2. Coupled data

Our data is taken from [27], where the Cassini ISS Narrow Angle Camera (NAC) plume photos are analyzed and intensities from the pixel values in the images are calculated. However, these intensities are in terms of Equivalent Width (EW), which is a niche quantity primarily used in planetary ring studies.

EW is often used because it accounts for the background subtraction of other illuminated objects, as well as issues such as a celestial object being smaller than the resolution of the detector.

The EW can be treated as an intensity, even though it has different units. It is defined as an integral of the reflectance of the scatterers in a cloud of particles and uses the fact that the power received by a detector must be equal to the power scattered by the cloud. See [28] for a more in depth explanation and derivation. As mentioned in [19,29], the EW can be defined as:

$$EW(\Theta, N) = \int \frac{I}{F} dxdy = \frac{NA_p Q_{sca} P(\theta)}{4} \tag{2}$$

Where N is the number of particles, $A_p$is the cross-sectional area of each particle, Q_{sca} is the scattering efficiency and $P(\theta)$ is the phase function. I is the intensity (radiance) measured at the detector, and F is the incident solar flux, also known as irradiance, making I/F the reflectance of the scatterers.

The authors of [27] measure the I/F values in a line of pixels perpendicular to Enceladus' rotation axis and then multiply by the projected pixel size, perpendicular to the line of sight at the distance to the Enceladus center, in km. Therefore, x is the distance along the line of pixels, so EW is given in units of km. As the plumes are optically thin, the EW accounts for all the light from the particles in a horizontal plane one projected pixel thick at the altitude of the line of pixels in the image, at an altitude of 100 km.

Using the formulas for the scattering quantities such as the scattering efficiency $Q_{sca}$and phase function $P(\theta)$allow us to reduce the EW further [30].

$$Q_{sca} = \frac{C_{sca}}{A_p} \tag{3}$$

$$\text{and } P(\theta) = \frac{4\pi S_{11}(\Theta)}{C_{sca} k^2} \tag{4}$$

Combining Eqs. (2)-(4) and simplifying gives:

$$EW(\Theta, N) = \int \frac{I}{F} dxdy = \frac{NA_p \frac{C_{sca}}{A_p} 4\pi S_{11}(\Theta)}{4 C_{sca} k^2} \tag{5}$$

Or

$$EW(\Theta, N) = \int \frac{I}{F} dxdy = \frac{N\pi S_{11(\Theta)}}{k^2} \tag{6}$$

Eq. (6) is now in terms of the S11 element of the Mueller scattering matrix, which can be calculated by the light scattering simulation codes, Amsterdam Discrete Dipole Approximation (ADDA) and T-Matrix [31,32]. This is necessary for comparing the satellite data to light scattering simulations. This reduction also removes the particle area term, which is an unknown quantity. The wavenumber k is known because the central wavelength λ of each filter is known. The number of particles, N, creates a problem, however, as the particles present in an image are not countable, a complication addressed below.

2.1. Reduction

As Cassini flies by Enceladus multiple times, the satellite records data at multiple orbit locations. The mean anomaly M of Enceladus can be

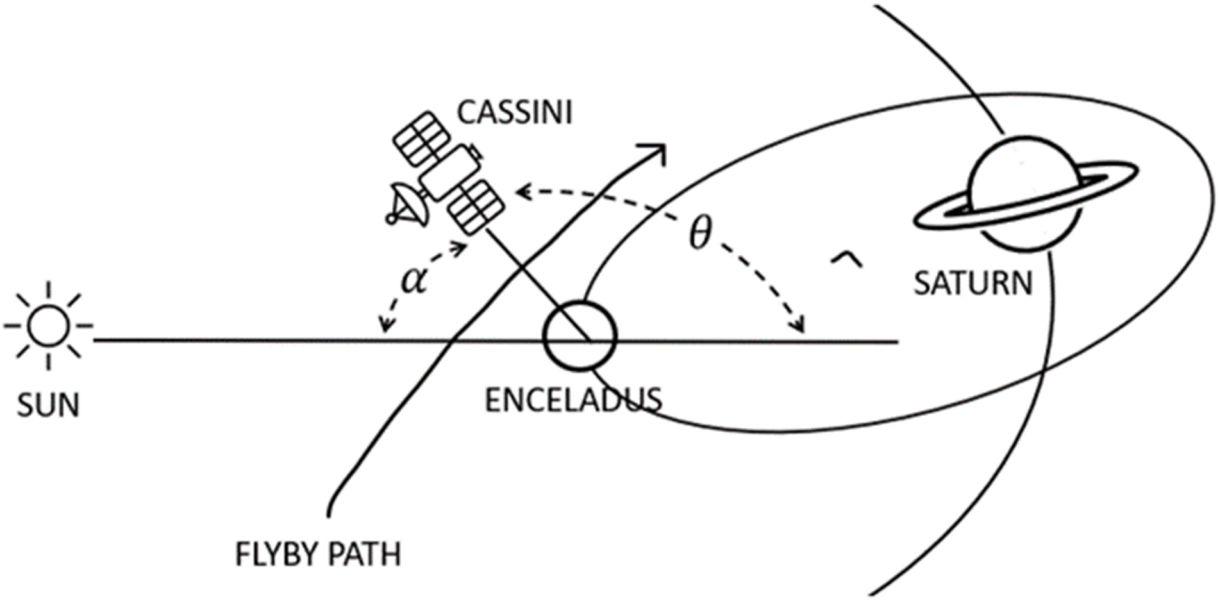

Fig. 1. Geometry of the Sun-Enceladus-Cassini-Saturn system where the eccentricity of Enceladus' orbit has been exaggerated for clarity. Saturn orbits the sun, Enceladus orbits Saturn, and during a flyby, Cassini orbits Enceladus. Relative to Enceladus, Cassini has a hyperbolic orbit with a large eccentricity, causing the orbit to appear almost as a straight line. Enceladus is pictured at the apocenter of its orbit around Saturn for clarity, as well. Enceladus is situated within Saturn's tenuous E-ring and is not as distant as the diagram depicts. The phase angle α is the Sun-Enceladus-detector angle, and the scattering angle Θ is the angle through which sunlight is scattered. Thus, we see that Θ=180° - α. The cryovolcano plumes on Enceladus are most visible at scattering angles of Θ<40°, but images are recorded over a much larger range of angles.

thought of as where Enceladus is around Saturn if its elliptical orbit is mapped to a circle with one constant average speed. Since Enceladus has a low eccentricity of 0.005 [29], its mean anomaly is very similar to its true anomaly. Mean anomaly of $M = 0^\circ$ is defined to be at periapsis, and $M = 180^\circ$ is defined as being at apoapsis. Plotting EW versus M, Fig. 2 below, shows the systematic behavior of the plumes as Enceladus orbits. One might assume that if the only mechanism for increasing cryovolcanic activity is tidal forces from Saturn, then the greatest EW should be at periapsis, as that is when Enceladus is closest to Saturn. However, models such as [33] show that the stress on the faults of Enceladus' South Pole may peak near apoapsis. The fact that the EW peaks when Enceladus is furthest from Saturn implies that there are multiple effects causing the cryovolcanoes to erupt beyond simple tidal heating from Saturn.

The variation in EW between years likely comes from several sources, including Enceladus' 2:1 resonance with Dione [34,35]. Other possible sources may include Saturn's orbit around the sun or internal factors such as the structure of the vents (Ingersoll et al., 2020). Orbital resonances compound tidal forces, and often are sources of large amounts of internal energy, especially in the case of Enceladus where there are so many bodies in Saturn's ring system [5]. However, because Saturn's rings contain many bodies, it is difficult to calculate all the tidal forces acting on Enceladus at different times. One Saturn year takes 29.5 Earth years, and the planet precesses as it orbits [36]. As Enceladus is in the plane of Saturn's rings, Saturn's precession causes Enceladus to enter and exit the orbital plane of the solar system. Although, the effects of Saturn's orbital eccentricity and obliquity are much smaller than the effects of the other moons such as Dione [29].

The variability of EW within a single Enceladus orbit, which takes around 34 h [37], comes from the slight variation in the moon's distance from Saturn as well as the positions of the other moons. As the orbital distance changes, so does the strength of the tidal forces acting on Enceladus. Regardless of the source of the variation, Fig. 2 resembles a sinusoidal curve, and thus it is necessary to analyze the intensities accounting for this behavior.

Here we assume that the plume intensities vary with respect to M due to the changing tidal forces. The forces enhance or suppress the cryovolcano activity at certain points in the orbit, so that the intensity data is coupled with position. Ideally, EW should be a function only of Θ, but rather, it is a function of both Θ and N, see Eq. (6). Particle number, N, varies both on the short timescale of Enceladus's orbital period and the much longer, roughly decadal timescales comparable to the duration of Cassini's mission at Saturn as discussed in [27,29]. Thus, the pixel intensities are dependent on the activity of the cryovolcanoes. The more active they are, the more particles are present in the detector's line of sight, meaning that the images contain higher intensities. In other words:

$$EW(\Theta, N) = EW(N) \times EW(\Theta) \tag{7}$$

This must be uncoupled before any further light scattering analysis. In this work, this is done by deriving a correction factor from the 2017 data in Fig. 2 to apply to data throughout the mission.

In Fig. 3, we fit the 2017 data from Fig. 2 with a polynomial of order 15. Data from 2017 is used because the 2017 curve is nestled between the other years, implying a possible near average value in the decadal variability of the tidal forces. It also contains 1704 out of the total ~2500 data points, meaning high resolution for the fit. This specific polynomial was chosen by using Mathematica's built in fitting function, "Fit", and iterating through every order up to order 30. Order 15 was chosen by checking the residuals, and picking the lowest order polynomial that gave acceptable residuals and displayed convergence. This method is inspired by the one used in [27].

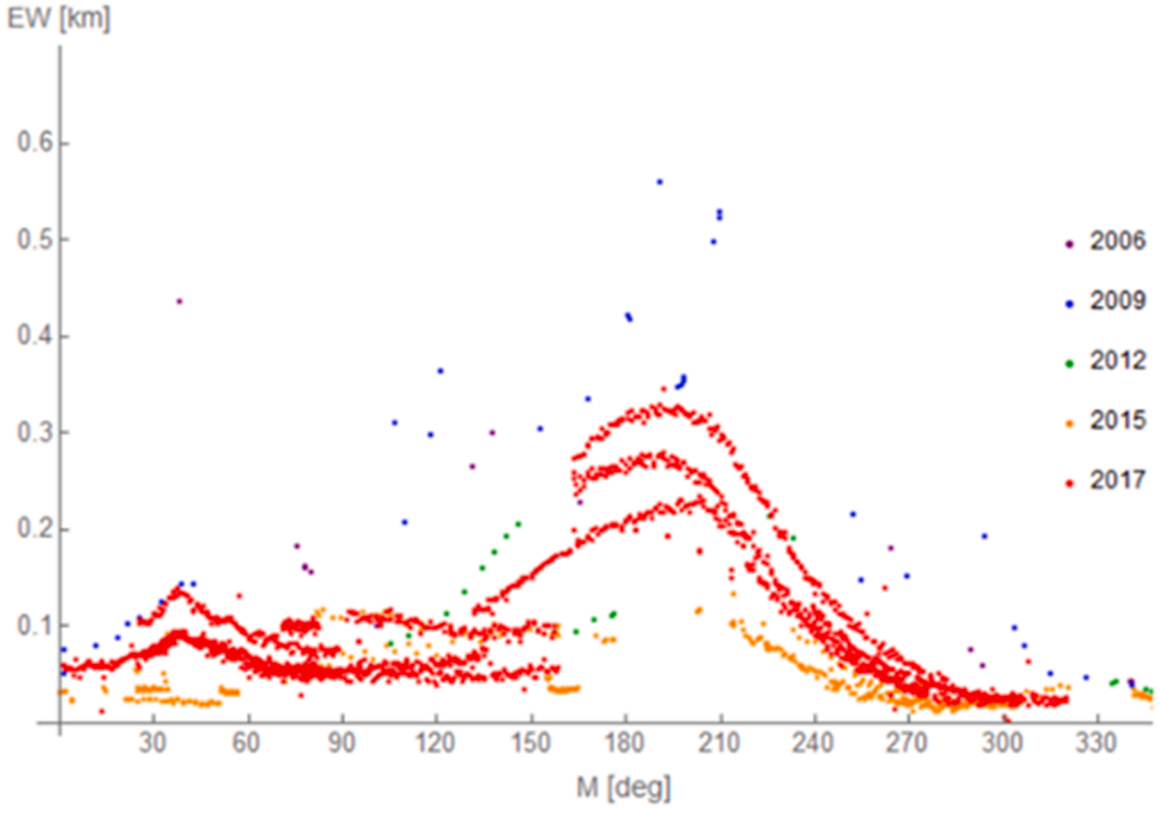

Fig. 2. Equivalent Width EW as a function of mean anomaly M as collected and analyzed by (Ingersoll et al., 2020). Each color represents a different year's dataset. If EW was only dependent on Θ and not M as well, the above plot would look random. Also, if the increase in cryovolcano activity as demonstrated by EW was only due to Saturn, there would be a maximum at $M = 0^\circ$ Instead, the nature of the second peak is currently unknown, but likely due to a combination of tidal forces and vent phenomena.

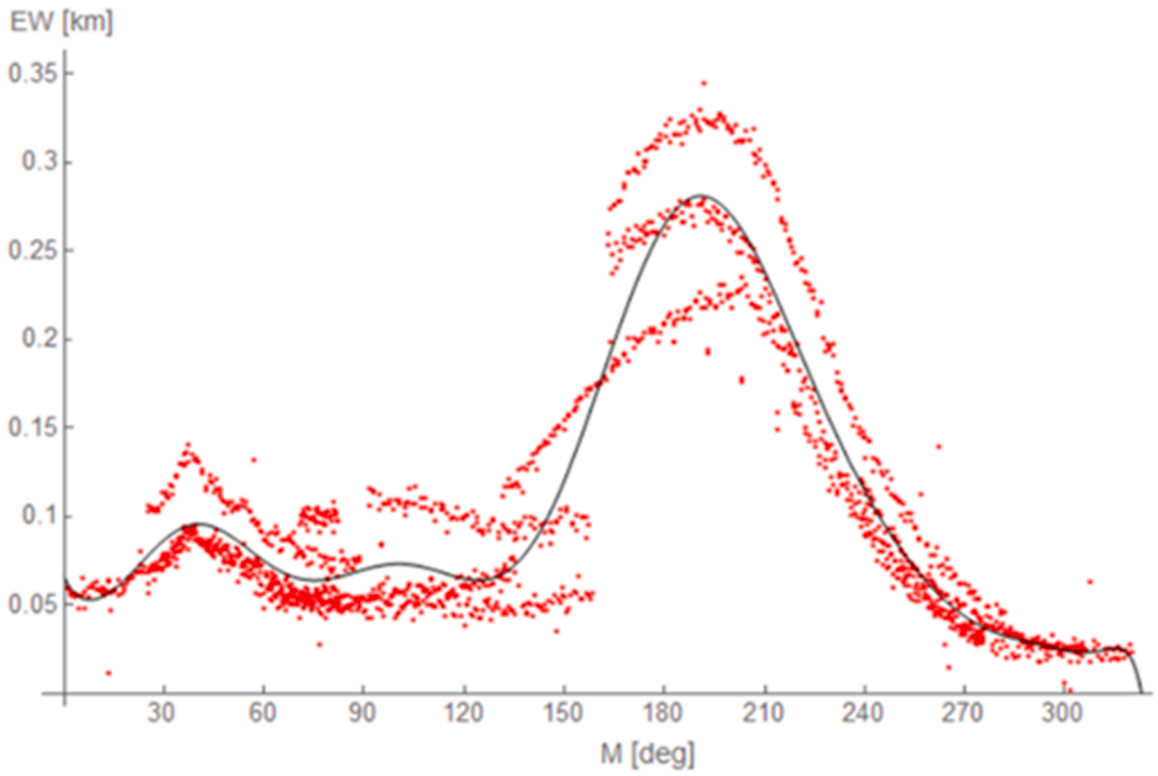

Fig. 3. The 2017 data from Fig. 2 now plotted and fit with a high-order polynomial curve. The fit is calculated using Wolfram Mathematica's built-in fitting function [38]. The fitted curve represents the behavior of the cryovolcano activity with respect to orbital position, and accounts for tidal resonances and other variable forces Enceladus experiences during its orbit.

To uncouple the data, we assume the number of particles, N, depends on the mean anomaly M due to tidal forces. As M is a measured quantity and N is not, only EW(M) is known, not EW(N(M)). We assume EW(M) to depend linearly on N.

$$EW(M) = CN(M) \tag{8}$$

where C is some constant.

We define a new quantity, "New Equivalent Width", or EW', to demonstrate the elimination of the mean anomaly dependence.

$$EW'(\Theta) = \frac{EW(\Theta, N)}{EW(M)} \tag{9}$$

We can combine Eqs. (8) - (9) into Eq. (10).

$$EW'(\Theta) = C\frac{EW(\Theta, N)}{N} \tag{10}$$

Plugging in Eq. (6) for EW(Θ,N) and simplifying results in Eq. (11), where EW' is now only a function of Θ and has no dependence on the orbital position of Enceladus nor the number of particles present in the plume.

$$EW'(\Theta) = C\frac{\pi S_{11}(\Theta)}{k^2} \tag{11}$$

Therefore, by dividing every years' data by the equation of the fitted curve in Fig. 3, EW(M), the particle number dependence is no longer an issue. If the EW was only a function of N (or M), then dividing by the curve in Fig. 3 would reduce everything to 1. However, this does not happen because of the scattering angle dependence.

This reduction works only if the behavior of the resulting curves is considered such as the slopes in certain regimes, not the actual values of EW' due to the constant that was introduced. Q-space analysis commonly utilizes normalized intensity values, meaning that the introduction of the constant C will not complicate this analysis.

The EW' versus Θ plot in Fig. 4(b) is much cleaner than the 2017 plot of the original averaged data, Fig. 4(a). To apply the curve reduction in Fig. (3) to other years, the errors are binned by scattering angle. This accounts for the narrow range of angles measured in the 2017 data and allows application to years with smaller angles. Error sources include Cassini instrument error, error from reduction of the images, and the fitting and division of the curve. The error is propagated, using the deviation of multiple points at a single scattering angle as a basis of the Cassini instrument error at each angle bin. The curve fits better at some points than others which is accounted for using the root-mean-square error (RMSE). Points outside three standard deviations of the mean are considered outliers and removed.

The data sets with the smallest recorded scattering angles are 2006 CLR, 2009 CLR, 2012 CLR, and 2012 BL1. The Cassini CLR filter is centered at λ=611 nm, whereas the BL1 filter is centered at λ=451 nm [39].

3. Q-SPACE analysis

The four data sets with the smallest measured scattering angles are plotted in Fig. (5). Small angles offer insight into the so-called Guinier regime, which allows for simple estimation of the average particle size by identifying the Guinier point, or where the points plateau at the smallest angle [42]. These plots do not show such behavior, however, implying that the particles are larger than the minimum inverse q present in the data. Here, the smallest q is $q_{min} = 0.43\mu m^{-1}$, corresponding to particle radii $>1/q_{min} = 2.3\ \mu m$. The particles in Enceladus' plumes are most likely present in a size distribution as opposed to being monodisperse. This simple length-scale argument sets the minimum average radii for the particles in the distribution to be greater than 2.3 μm.

In [10], the plume particles are assumed to follow power law size distributions of $dN/dR = R^{-q}$. For their preferred case of $q = 3$, they determine that the median radius in terms of scattering cross-section to

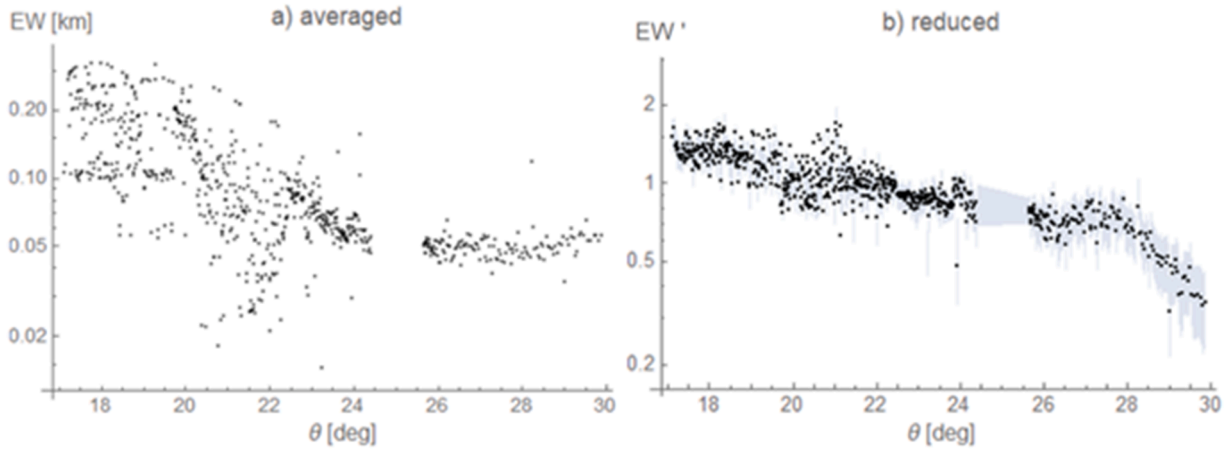

Fig. 4. The EW 2017 data from Fig. 2, before and after the division of the curve in Fig. 3, now plotted logarithmically against Θ. Plot (a) has duplicate scattering angle measurements averaged to a single point. Plot (b) has outliers removed. After this removal, the error ranges from 20 to 40 % of the EW' value and is shown as the gray band. Plot (a) does not resemble a typical light scattering curve due to its high amount of scatter between the points. Plot (b) is cleaner and follows the expected shape of a light scattering curve. Unfortunately, the 2017 data does not contain measurements at very low Θ. The y-axis values differ due to the constant that was introduced in the reduction.

be 1.206 μm, with 90% of the particle radii in the distribution to be between 0.274 and 8.028 μm. However, in a secondary case with $q = 4$, the median radius is found to be lower at r_{med}= 0.488 μm with 90 % of the cross-section in particles with radii between 0.134 and 2.771 μm. The scattering cross-sections are converted into particle radii via Mie simulations, meaning the particles are assumed to be spheres. The authors of [10] use a much different functional form for the modelled size distribution, assume the particles are spherical or oblate and prolate spheroids, and find a mean volume-equivalent sphere radius of 3.1 μm. While the results of this paper are similar to the particle sizes determined in the aforementioned papers, Q-space analysis of size is shape independent [41].

Another important quantity for Q-space analysis is the internal coupling parameter of a sphere ρ',

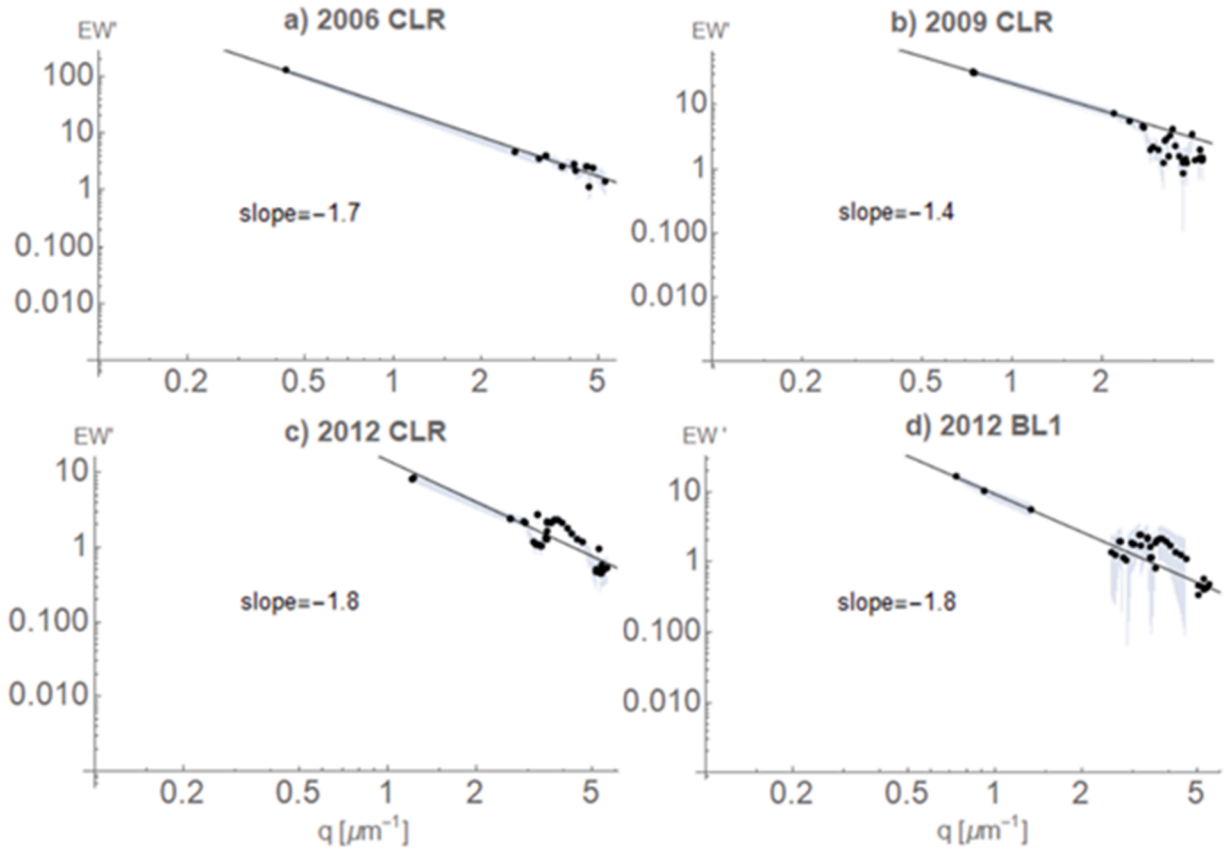

Fig. 5. The datasets with the smallest measured scattering angles as plotted on a log-log scale in Q-space. The 2006 observations in the CLR filter have a minimum scattering angle of 2.4°, and the 2009 CLR, 2012 CLR, and 2012 BL1 data sets have minimum angles of 4.11°, 6.76°, and 4.15° respectively. The slopes of the plots (a)-(d) are −1.7, −1.4, −1.8, and −1.8. These slopes imply a possibility of the particles being fractal aggregates or hexagonal columns, according to [40,41], but more work is needed to justify such conclusions.

$$\rho' = 2kR\left|\frac{m^2-1}{m^2+2}\right|, \quad (12)$$

where R is the radius of a sphere and m is the complex refractive index [43].

When $\rho' < 1$, the electromagnetic coupling within a particle is weak. In other words, internal multiple scattering is weak, and thus the scattering is in the Rayleigh-Debye-Gans limit, which corresponds to diffraction from the volume of the particle. The Rayleigh-Debye-Gans limit, sometimes called the Rayleigh-Debye-Gans approximation, refers to scattering by optically soft particle, or when the refractive index of the particle is similar to the surrounding medium [30]. As ρ' increases, so does the coupling and the scattering corresponds then to diffraction from the particle's projected area (profile), i.e. 2D diffraction, see [42].

The ρ' parameter is helpful to compare slopes of different particles in Q-space by separating them into coupling regimes. Assuming the particles in the cryovolcanoes are ice ($m = 1.309 + 7.096 \times 10^{-9}i$ at λ=0.611 μm) [44], and constraining $R > 2$ μm, gives $\rho' > 7.92$. Comparing to Fig. 1 in [40] shows that these particles potentially are not spherical, as spheres have slopes of −2 in ρ' regimes less than 10, and the slopes from the Cassini data range from −1.4 to −1.8. Even if the particles are not ice, spheres follow the same general behaviors in Q-space regardless of m. Spheres with ρ'=8 with varying refractive indices are plotted below (Fig. 6), with lines of slope=−2 and −3 for reference. A solid line with slope −1.7 is also plotted, as a reference to the curves in Fig. 5. Slopes between −1 and −2 have been found to occur for various types of irregular particles such as Saharan dust or minerals [41].

4. Conclusion

The Q-space approach is especially useful in remote sensing problems, and its simple nature makes it ideal for space applications. This work removes the particle number effect on Enceladus' intensity measurements and applies Q-space analysis to the data. Using the Q-space method, the particles are constrained to be greater than 2.3 μm in size and have been shown to likely not be spherical in that size range.

Future work envisions simulating possible particle shapes and size distributions in ADDA and T-matrix and comparing the results to the reduced data to improve conclusions about the plume properties from a light scattering perspective.

CRediT authorship contribution statement

Claudia Morello: Writing – review & editing, Writing – original draft, Visualization, Validation, Resources, Project administration, Methodology, Investigation, Formal analysis, Data curation, Conceptualization. **Matthew J. Berg:** Writing – review & editing, Writing – original draft, Supervision, Resources, Project administration, Funding acquisition, Formal analysis.

Declaration of competing interest

The authors declare the following financial interests/personal relationships which may be considered as potential competing interests: Claudia Morello reports financial support was provided by Kansas State University. Claudia Morello reports a relationship with Kansas State University that includes: employment.

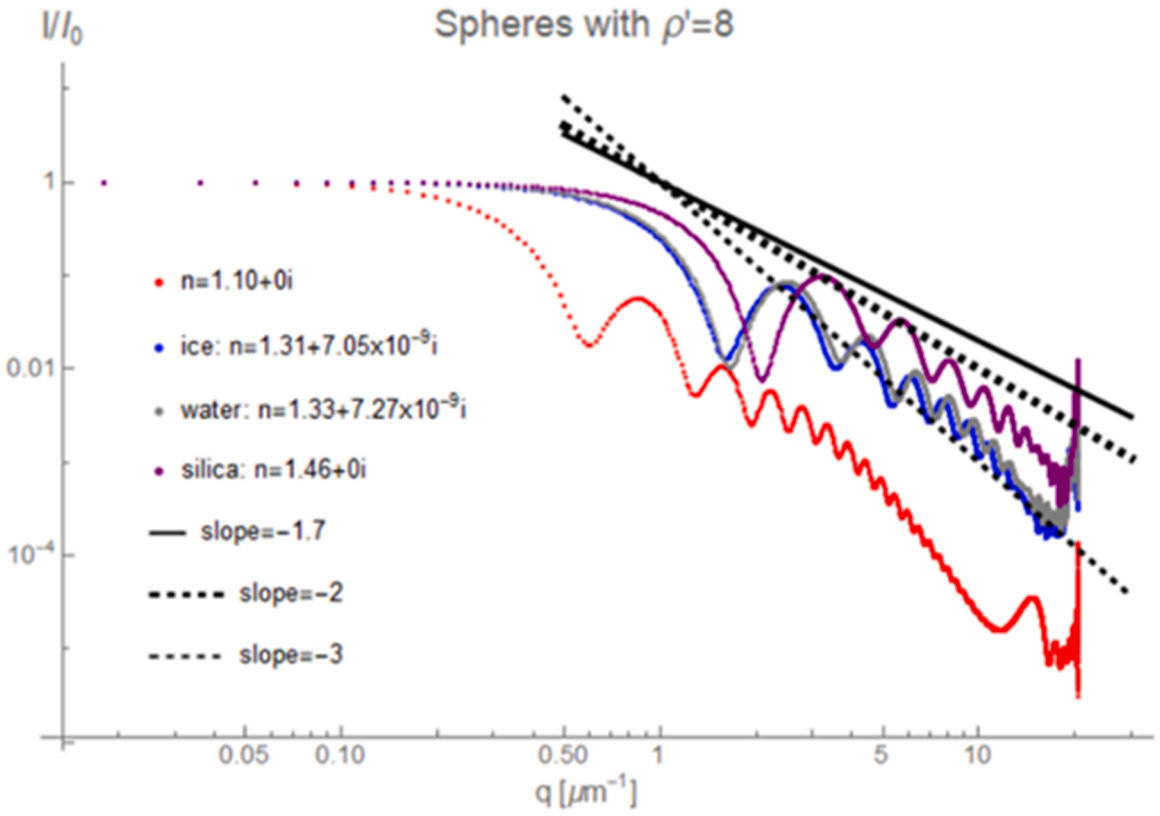

Fig. 6. Spheres of varying refractive indices from silica to liquid water and water ice [44], plotted in Q-space with normalized intensity for ρ'=8 . These substances were chosen because they may be present in the plumes. A curve for $m = 1.1 + 0i$ is also plotted, to show that the slopes are not dependent on m even for low m. These were simulated in Philip Laven's MiePlot [45] using λ=611 nm (Cassini's CLR filter), and varying R. Slight size distributions (20 % variation) were used to reduce the interference ripples. This plot builds off Fig. 1 in [40], which finds that spheres in various ρ' regimes have slopes of −2 and −3, regardless of R. It is important to note that solid materials with $m < 1.1$ are not naturally occurring [46].

Data availability

The data used comes from a different group and is explained in the paper with references.

Acknowledgements

This research was supported by the US Air Force Office of Scientific Research grants FA9550-19-0078 and FA9550-21-1-0339, the National Science Foundation grant 2107715, and the US Army Research Office grant W911NF2120053. We acknowledge helpful advice from Christopher Sorensen, Luke Dones, Justin Maughan, Robert West, and Evgenij Zubko.

References

[1] Hedman MM, Burns JA, Hamilton DP, Showalter MR. The three-dimensional structure of Saturn's E ring. Icarus 2012;217(1):322–38. https://doi.org/10.1016/j.icarus.2011.11.006.
[2] Hill TW. Saturn's E ring. Adv Space Res 1984;4(9):149–57. https://doi.org/10.1016/0273-1177(84)90020-6.
[3] Showalter MR, Cuzzi JN, Larson SM. Structure and particle properties of Saturn's E Ring. Icarus 1991;94(2):451–73. https://doi.org/10.1016/0019-1035(91)90241-K.
[4] "Saturn Moons - NASA Science." Accessed: Oct. 10, 2023. [Online]. Available: https://science.nasa.gov/saturn/moons/.
[5] Porco C, DiNino D, Nimmo F. How the Geysers, Tidal Stresses, and thermal emission across the south polar terrain of Enceladus are related. Astron J 2014;148(3):45. https://doi.org/10.1088/0004-6256/148/3/45.
[6] Porco CC, et al. Cassini Observes the Active South Pole of Enceladus. Science 2006;311(5766):1393–401. https://doi.org/10.1126/science.1123013.
[7] Iess L, et al. The gravity field and interior structure of enceladus. Science 2014;344(6179):78–80. https://doi.org/10.1126/science.1250551.
[8] Thomas PC, et al. Enceladus's measured physical libration requires a global subsurface ocean. Icarus 2016;264:37–47. https://doi.org/10.1016/j.icarus.2015.08.037.
[9] Martin W, Baross J, Kelley D, Russell MJ. Hydrothermal vents and the origin of life. Nat Rev Microbiol 2008;6(11):11. https://doi.org/10.1038/nrmicro1991. Art. no.
[10] Porco CC, Dones L, Mitchell C. Could It Be Snowing Microbes on Enceladus? Assessing Conditions in Its Plume and Implications for Future Missions. Astrobiology 2017;17(9):876–901. https://doi.org/10.1089/ast.2017.1665.
[11] Mitchell CJ, Porco CC, Weiss JW. Tracking the Geysers of Enceladus into Saturn's E-Ring. Astron J 2015;149(5):156. https://doi.org/10.1088/0004-6256/149/5/156.
[12] Filacchione G, et al. Saturn's icy satellites investigated by Cassini – VIMS. V. Spectrophotometry. Icarus 2022;375:114803. https://doi.org/10.1016/j.icarus.2021.114803.
[13] Hendrix AR, Hansen CJ, Holsclaw GM. The ultraviolet reflectance of Enceladus: implications for surface composition. Icarus 2010;206(2):608–17. https://doi.org/10.1016/j.icarus.2009.11.007.
[14] Verbiscer AJ, et al. Near-infrared spectra of the leading and trailing hemispheres of Enceladus. Icarus 2006;182(1):211–23. https://doi.org/10.1016/j.icarus.2005.12.008.
[15] Gao P, Kopparla P, Zhang X, Ingersoll AP. Aggregate Particles in the Plumes of Enceladus. Icarus 2016;264:227–38. https://doi.org/10.1016/j.icarus.2015.09.030.
[16] Nimmo F, Porco C, Mitchell C. Tidally Modulated Eruptions on Enceladus: cassini ISS Observations and Models. Astron J 2014;148(3):46. https://doi.org/10.1088/0004-6256/148/3/46.
[17] Poch O, Cerubini R, Pommerol A, Jost B, Thomas N. Polarimetry of Water Ice Particles Providing Insights on Grain Size and Degree of Sintering on Icy Planetary Surfaces. J. Geophys. Res. Planets 2018;123(10):2564–84. https://doi.org/10.1029/2018JE005753.
[18] Sorensen CM, Fischbach DJ. Patterns in Mie scattering. Opt Commun 2000;173(1):145–53. https://doi.org/10.1016/S0030-4018(99)00624-0.
[19] Ingersoll AP, Ewald SP. Total particulate mass in Enceladus plumes and mass of Saturn's E ring inferred from Cassini ISS images. Icarus 2011;216(2):492–506. https://doi.org/10.1016/j.icarus.2011.09.018.
[20] Jaumann R, et al. Distribution of icy particles across Enceladus' surface as derived from Cassini-VIMS measurements. Icarus 2008;193(2):407–19. https://doi.org/10.1016/j.icarus.2007.09.013.
[21] Waite JH, et al. Cassini Ion and Neutral Mass Spectrometer: enceladus Plume Composition and Structure. Science 2006;311(5766):1419–22. https://doi.org/10.1126/science.1121290.
[22] Khawaja N, et al. Low-mass nitrogen-, oxygen-bearing, and aromatic compounds in Enceladean ice grains. Mon Not R Astron Soc 2019;489(4):5231–43. https://doi.org/10.1093/mnras/stz2280.
[23] Postberg F, et al. Sodium salts in E-ring ice grains from an ocean below the surface of Enceladus. Nature 2009;459(7250):7250. https://doi.org/10.1038/nature08046. Art. no.
[24] Hsu H-W, et al. Ongoing hydrothermal activities within Enceladus. Nature 2015;519(7542):7542. https://doi.org/10.1038/nature14262. Art. no.
[25] Postberg F, et al. Detection of phosphates originating from Enceladus's ocean. Nature 2023;618(7965):7965. https://doi.org/10.1038/s41586-023-05987-9. Art. no.
[26] Peter JS, Nordheim TA, Hand KP. Detection of HCN and diverse redox chemistry in the plume of Enceladus. Nat Astron 2024;8(2):164–73. https://doi.org/10.1038/s41550-023-02160-0.
[27] Ingersoll AP, Ewald SP, Trumbo SK. Time variability of the Enceladus plumes: orbital periods, decadal periods, and aperiodic change. Icarus 2020;344:113345. https://doi.org/10.1016/j.icarus.2019.06.006. Jul.
[28] Scharringhausen BR. A photometric model of the inclined f ring of saturn. Cornell University; 2007. Jan.[Online]. Available: https://ecommons.cornell.edu/bitstream/handle/1813/3707/main.pdf?sequence=1&isAllowed=y.
[29] Ingersoll AP, Ewald SP. Decadal timescale variability of the Enceladus plumes inferred from Cassini images. Icarus 2017;282:260–75. https://doi.org/10.1016/j.icarus.2016.09.018.
[30] C.F. Bohren and D.R. Huffman, "Absorption and scattering of light by small particles," 1983. Accessed: Jun. 09, 2023. [Online]. Available: https://ui.adsabs.harvard.edu/abs/1983uaz..rept.....B.
[31] Mackowski DW, Mishchenko MI. A multiple sphere T-matrix Fortran code for use on parallel computer clusters. J Quant Spectrosc Radiat Transf 2011;112(13):2182–92. https://doi.org/10.1016/j.jqsrt.2011.02.019.
[32] Yurkin MA, Hoekstra AG. The discrete-dipole-approximation code ADDA: capabilities and known limitations. J Quant Spectrosc Radiat Transf 2011;112(13):2234–47. https://doi.org/10.1016/j.jqsrt.2011.01.031.
[33] Hurford TA, Helfenstein P, Hoppa GV, Greenberg R, Bills BG. Eruptions arising from tidally controlled periodic openings of rifts on Enceladus. Nature 2007;447(7142):7142. https://doi.org/10.1038/nature05821. Art. no.
[34] Meyer J, Wisdom J. Tidal evolution of Mimas, Enceladus, and Dione. Icarus 2008;193(1):213–23. https://doi.org/10.1016/j.icarus.2007.09.008.
[35] Vienne A, Duriez L. A general theory of motion for the eight major satellites of Saturn. III - Long-period perturbations. Astron Astrophys 1992;257:331–52.
[36] J. Wisdom et al., "Loss of a satellite could explain Saturn's obliquity and young rings." Accessed: Jun. 09, 2023. [Online]. Available: https://www.science.org/doi/10.1126/science.abn1234.
[37] "Enceladus, " NASA Solar System Exploration. Accessed: Jun. 09, 2023. [Online]. Available: https://solarsystem.nasa.gov/moons/saturn-moons/enceladus/in-depth.
[38] Wolfram Research, Inc. Mathematica. Wolfram Research, Inc; 2023 [Online]. Available: https://www.wolfram.com/mathematica.
[39] Porco CC, et al. Cassini Imaging Science: instrument Characteristics And Anticipated Scientific Investigations At Saturn. Space Sci Rev 2004;115(1):363–497. https://doi.org/10.1007/s11214-004-1456-7.
[40] Heinson YW, Maughan JB, Ding J, Chakrabarti A, Yang P, Sorensen CM. Q-space analysis of light scattering by ice crystals. J Quant Spectrosc Radiat Transf 2016;185:86–94. https://doi.org/10.1016/j.jqsrt.2016.08.021.
[41] Sorensen C, Heinson Y, Heinson W, Maughan J, Chakrabarti A. Q-Space Analysis of the Light Scattering Phase Function of Particles with Any Shape. Atmosphere (Basel) 2017;8(4):68. https://doi.org/10.3390/atmos8040068.
[42] Sorensen CM. Q-space analysis of scattering by particles: a review. J Quant Spectrosc Radiat Transf 2013;131:3–12. https://doi.org/10.1016/j.jqsrt.2012.12.029.
[43] Heinson WR, Chakrabarti A, Sorensen CM. A new parameter to describe light scattering by an arbitrary sphere. Opt Commun 2015;356(December 2015):612–5. https://doi.org/10.1016/j.optcom.2015.08.067.
[44] Warren SG, Brandt RE. Optical constants of ice from the ultraviolet to the microwave: a revised compilation. J Geophys Res 2008;113(D14):D14220. https://doi.org/10.1029/2007JD009744.
[45] P. Laven, "MiePlot." Accessed: Aug. 04, 2023. [Online]. Available: http://www.philiplaven.com/mieplot.htm.
[46] Zhang XA, et al. Ordered 3D Thin-Shell Nanolattice Materials with Near-Unity Refractive Indices. Adv Funct Mater 2015;25(42):6644–9. https://doi.org/10.1002/adfm.201502854.